









## Light-induced enhancement of superconductivity in iron-based superconductor $\text{FeSe}_{0.5}\text{Te}_{0.5}$

Kazuki Isoyama<sup>1</sup>, Naotaka Yoshikawa<sup>1</sup> , Kota Katsumi<sup>1</sup> , Jeremy Wong<sup>1</sup> , Naoki Shikama<sup>2</sup> , Yuki Sakishita<sup>2</sup> , Fuyuki Nabeshima<sup>2</sup> , Atsutaka Maeda<sup>2</sup>  & Ryo Shimano<sup>1,3</sup> ✉

Illumination of light on matter normally causes heating and destroys the ordered ground states. Despite this common understanding, recent advances in ultrafast light sources have enabled the non-thermal control of quantum phases. Here, we report the light-induced enhancement of superconductivity in a thin film of an iron chalcogenide  $\text{FeSe}_{0.5}\text{Te}_{0.5}$ , which exhibits multiple quantum condensates associated with the multi-orbital character. Upon the photoexcitation, we observed a transient increase of the superfluid density as indicated by the optical conductivity in the frequency range of superconducting gaps. The light-induced enhancement of superconductivity is further corroborated by the photoinduced enhancement of terahertz third harmonic generation, which is accounted for by the Higgs mode response. The ultrafast dynamics of two superfluid components revealed by frequency- and time-resolved terahertz measurements indicate the interplay between the condensates through the interband Cooper pairings while suggesting the potential tunability of the pairing interaction by light in the ultrafast timescale.

<sup>1</sup>Department of Physics, The University of Tokyo, Tokyo, Japan. <sup>2</sup>Department of Basic Science, The University of Tokyo, Tokyo, Japan. <sup>3</sup>Cryogenic Research Center, The University of Tokyo, Tokyo, Japan. ✉email: [shimano@phys.s.u-tokyo.ac.jp](mailto:shimano@phys.s.u-tokyo.ac.jp)

The discovery of iron-based superconductors (FeSCs) has opened a new paradigm of research of high critical temperature superconductors<sup>1,2</sup>. One common nature of FeSCs is that all the five Fe's 3d orbitals participate in the Fermi surfaces, constituting multiple Fermi pockets, typically those of hole bands around the zone center ( $\Gamma$  point) and electron bands around the zone edge (M point) in momentum space. The electronic nematicity and interband Cooper pairings arising from the multiband character are considered as crucial ingredients for the understanding of the emergent superconductivity. Among the variety of FeSCs discovered to date, much attention has been focused on FeSe and its related compounds in recent years<sup>3,4</sup>. One intriguing aspect of this material is the high tunability of the superconducting critical temperature ( $T_c$ ):  $T_c \sim 9$  K of FeSe under ambient pressure is boosted to about 38 K under high pressure of 6 GPa<sup>5</sup>.  $T_c$  of  $> 30$  K is also archived by electron doping via intercalation or ionic-liquid gating<sup>6–9</sup>. Strikingly,  $T_c$  reaches even 65 K in a monolayer FeSe grown on SrTiO<sub>3</sub> substrate as estimated from the gap closing temperature in angle-resolved photoemission spectroscopy (ARPES)<sup>10–12</sup>. The isovalently substituted compounds, FeSe<sub>1–x</sub>Te<sub>x</sub> and FeSe<sub>1–x</sub>S<sub>x</sub>, have also been studied intensively to elucidate the interplay between the superconductivity and the electronic nematicity<sup>13–16</sup>. The Fermi energies for both electron and hole bands are shown to be exceptionally small and comparable to the superconducting gaps, and notably, a clear correlation between  $T_c$  and the Fermi surface topology has been revealed from the ARPES study with tuning the chemical potential by the surface dosing<sup>17</sup>. Different from these static tunings, one can consider the dynamical tuning by strong photoexcitation as an alternative route to control the superconductivity and other competing or coexisting orders. Indeed, recent ultrafast laser spectroscopic measurements have shown the transient appearance of a spin density wave phase<sup>18</sup> and the photoinduced melting of the nematic order<sup>19–21</sup>. Recently, a gap opening around the Fermi level was indicated in the time-resolved ARPES measurement under strong photoexcitation above  $T_c$  and interpreted as light-induced superconductivity<sup>22</sup>, providing a new aspect of photoinduced superconducting phenomena so far reported in cuprate superconductors<sup>23–25</sup> and organic conductors<sup>26–28</sup>. To prove the superconductivity, however, it is inevitable to confirm further fingerprints of superconductivity such as the Meissner effect, zero resistivity, and collective modes associated with the superconducting order parameter.

In the present work, we studied the effect of photoexcitation in thin films of FeSe<sub>0.5</sub>Te<sub>0.5</sub> that does not show the nematic order<sup>14</sup> by utilizing optical pump–terahertz (THz) probe spectroscopy. When the sample is excited by near-infrared (NIR) pulse below  $T_c$ , a transient increase of the superfluid density was observed after the photoexcitation as indicated by the  $1/\omega$ -like divergent behavior in the imaginary part of the optical conductivity. The enhancement of the superconducting order parameter is further corroborated by the THz-third-harmonic generation (THG) signal, which is accounted for by the Higgs mode response.

## Results

**Optical responses in equilibrium.** The band structure of FeSe<sub>0.5</sub>Te<sub>0.5</sub>, consisting of the hole bands at the  $\Gamma$  point and the electron bands at the M point<sup>29,30</sup>, is schematically shown in Fig. 1a. The tetragonal crystal structure of FeSe<sub>0.5</sub>Te<sub>0.5</sub> is also sketched in Fig. 1b. The thin film sample of FeSe<sub>0.5</sub>Te<sub>0.5</sub>, oriented along the *c*-axis, was epitaxially grown on a CaF<sub>2</sub> substrate by pulsed laser deposition method using a KrF laser. Figure 1c, d show the real and imaginary part of the complex optical conductivity spectrum,  $\tilde{\sigma}(\omega) = \sigma_1 + i\sigma_2$ , respectively, at various

temperatures obtained by time-domain THz spectroscopy. Below  $T_c = 16$  K defined by the zero resistivity (Fig. 1e), a missing of the spectral weight is observed in the real-part optical conductivity ( $\sigma_1$ ) in the range of 1–10 meV, indicating the opening of the superconducting gap with the gap size of  $\sim 10$  meV. A downturn below 4 meV in  $\sigma_1$  is also discerned at 4.3 K, suggesting the presence of a smaller superconducting gap. Namely, the two superconducting gaps in our FeSe<sub>0.5</sub>Te<sub>0.5</sub> sample are estimated as  $2\Delta_L \sim 10$  meV and  $2\Delta_S \leq 4$  meV, respectively. These values reasonably agree with the literature values of  $2\Delta_L = 7$ –11 meV and  $2\Delta_S = 2$ –5 meV, evaluated from ARPES<sup>29</sup>, infrared spectroscopy<sup>31,32</sup>, and scanning tunneling spectroscopy<sup>33,34</sup>. According to the ARPES study, the large gap ( $2\Delta_L$ ) is attributed to that of the electron bands around the M point and the small gap ( $2\Delta_S$ ) to the hole bands around the  $\Gamma$  point<sup>29</sup>. This assignment is also consistent with our analysis of the optical conductivity above  $T_c$  based on the two-component Drude model representing the hole and the electron bands (details are described in Supplementary Note 1), which suggests that the spectral weight around 10 meV is dominated by the electrons at the M point. The development of superconductivity below  $T_c$  is also indicated by the divergent behavior toward the zero-frequency limit in the  $\sigma_2$  spectrum (Fig. 1d). To discriminate the contribution from the Drude components of the normal state carriers, we fit the data in the low-frequency range of  $\hbar\omega = 1$ –2 meV with the two-fluid model,  $\sigma_2(\omega) = \epsilon_0 \omega_p^2 \omega / (\omega^2 + \gamma^2) + n_s / \omega$ , where  $\epsilon_0$  is the vacuum permittivity,  $\omega_p$  is the plasma frequency,  $\gamma$  is the damping rate, and  $n_s$  is the superfluid density, respectively. The extracted temperature dependence of  $n_s$ , which includes the contribution from both the hole and electron bands, i.e.,  $n_s = n_{s,S} + n_{s,L}$ , is shown in Fig. 1f.

**Transient optical conductivity.** Next, we measured the transient optical conductivity under the photoexcitation by utilizing optical pump and THz probe spectroscopy (Fig. 2a). As a pump source, we used the output of a regenerative amplifier system with the center photon energy of 1.55 eV, the pulse width of 90 fs, and the repetition rate of 1 kHz. Further details of THz spectroscopy are described in the “Methods” section. The temporal evolution of the real and imaginary part of the photoinduced conductivity change,  $\Delta\tilde{\sigma}(\omega; t_{pp}) = \tilde{\sigma}(\omega; t_{pp}) - \tilde{\sigma}^{eq}(\omega)$ , measured at 4.3 K are shown in Fig. 2b, c, respectively, as a function of pump–probe delay time,  $t_{pp}$ . Remarkably,  $\Delta\sigma_2(\omega; t_{pp})$  exhibits an enhancement from the equilibrium value right after the photoexcitation particularly in the low-frequency region at  $\hbar\omega \leq 2$  meV. This enhancement of  $\sigma_2$ , suggesting the enhancement of the superfluid density associated with the hole bands, is highlighted in the complex conductivity spectrum  $\tilde{\sigma}(\omega; t_{pp})$  taken at  $t_{pp} = 1.4$  ps (Fig. 2d) and the corresponding photoinduced conductivity change in the imaginary part  $\Delta\sigma_2(\omega; t_{pp})$  (Fig. 2e). Concomitantly,  $\sigma_1$  increases particularly in the low-energy region in the same temporal region (Fig. 2b, d). This increase of  $\sigma_1$  cannot be attributed to photoexcited carriers because  $\sigma_1$  remains almost unaffected under the photoexcitation at  $T > T_c$  (represented in Supplementary Fig. 2a) and the spectral weight increase due to the photoexcited carriers is negligible. Then, one may consider the superconducting quasiparticles caused by the photoexcitation, which should give a Drude-like spectrum at  $\hbar\omega \lesssim 2\Delta$ . However, this interpretation contradicts with the enhancement of the superfluid density as indicated by the  $1/\omega$ -like signal in  $\Delta\sigma_2$ . Accordingly, by taking into account the concomitant increase of the THG signal that will be discussed in the next section, we propose speculative scenarios that the observed low-energy behavior of  $\sigma_1$  reflects the character of the nonequilibrium

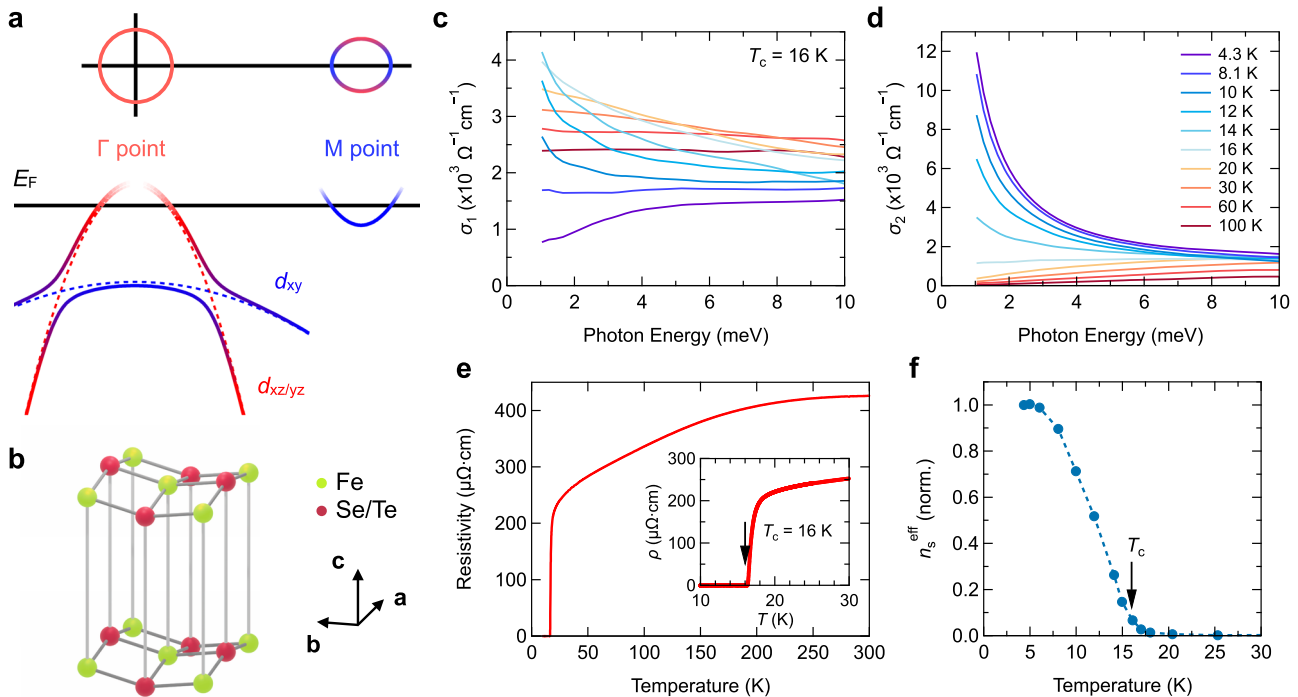


**Fig. 1 Temperature dependence of optical conductivity and resistivity of a thin film of FeSe<sub>0.5</sub>Te<sub>0.5</sub>.** **a** Schematic illustration of the band structure of FeSe<sub>0.5</sub>Te<sub>0.5</sub>, consisting of the hole bands at around the zone center ( $\Gamma$  point) and the electron bands at around the zone corner (M point)<sup>30</sup>. The iron  $d_{xz}$  and  $d_{yz}$  orbital characters are shown by red and the  $d_{xy}$  orbital is shown by blue. A schematic of the Fermi surface is also drawn at the top. **b** Schematic illustration of the crystal structure of FeSe<sub>0.5</sub>Te<sub>0.5</sub>. The crystal axes are indicated by the black arrows. The thin film sample of FeSe<sub>0.5</sub>Te<sub>0.5</sub>, oriented along the  $c$ -axis, was epitaxially grown on a CaF<sub>2</sub> substrate. **c, d** Optical conductivity spectra,  $\tilde{\sigma}(\omega) = \sigma_1(\omega) + i\sigma_2(\omega)$ , with the terahertz photon energy,  $\hbar\omega$ , at the indicated temperatures (**c**: real part; and **d**: imaginary part). The superconducting transition temperature ( $T_c$ ) is 16 K. **e** DC resistivity as a function of the temperature. Inset shows magnified data around  $T_c$ , defined by the zero resistivity. **f** Temperature dependence of the superfluid density,  $n_s^{\text{eff}}$ , extracted from the low-energy region of  $\sigma_2(\omega)$  ( $\hbar\omega < 2$  meV). The dashed line is a guide to the eye. The definition of  $n_s^{\text{eff}}$  is given in the text.

light-enhanced superconducting state. One possible reason may be attributed to the finite lifetime effect of the enhanced superconductivity. In this respect, it has been theoretically shown that the zero-frequency delta-function peak in  $\sigma_1$ , which corresponds to the superfluid response, broadens and exhibits a narrow Drude-like spectral profile when the enhancement of the superconducting order parameter is limited in a short period<sup>35</sup>. Another intriguing possibility is the recent theoretical proposal where an enhanced peak structure around the gap edge is predicted to emerge in the optical conductivity for a clean multiband superconductor possessing a spin-orbit interaction, as represented by FeSe<sup>36</sup>, which may also apply to the present case of FeSe<sub>0.5</sub>Te<sub>0.5</sub>. To elucidate whether such pictures apply to the present case of the photoinduced state, the observation of the optical conductivity spectra in the very low-energy range below  $\sim 1$  meV is needed, which remains a future subject.

Figure 2b, c also show  $\Delta\sigma_1(\hbar\omega_{\text{probe}} = 9.5$  meV;  $t_{\text{pp}})$  and  $\Delta\sigma_2(\hbar\omega_{\text{probe}} = 1.0$  meV;  $t_{\text{pp}})$  in their right panels, respectively. One can see that  $\Delta\sigma_2$  in the low-energy region increases with the rise time of 1.5 ps, and then, within 10 ps, evolves into a quasi-thermal state that lasts over 100 ps. The observed rise time reasonably agrees with the anticipated initial formation dynamics of superconductivity that is determined by the inverse of the superconducting gap energy, as theoretically discussed in a quantum quench problem in the Bardeen–Cooper–Schrieffer (BCS) mean-field framework<sup>37</sup> and more rigorously in the framework of the Migdal–Eliashberg approximation taking into account the electron–phonon coupling<sup>38</sup>. After the initial enhancement of  $\Delta\sigma_2$ , the complex optical conductivity becomes almost equivalent to the equilibrium optical conductivity

measured at 14 K within  $t_{\text{pp}} = 10$  ps as shown in Fig. 2f. This slow dynamics is consistent with the time-resolved optical reflectivity measurement<sup>19</sup> and the ultrafast electron diffraction measurement<sup>20</sup> and attributed to the thermalization process between the electron and lattice systems. It is worth noting that  $\sigma_1$  in the high-energy region remains intact in the initial 2 ps and subsequently approaches the normal state values, indicating that the superconductivity associated with the electron bands remains almost unchanged in the initial temporal region. We will discuss this reason later in detail.

**THG from superconducting phase of FeSe<sub>0.5</sub>Te<sub>0.5</sub>.** To further corroborate the light-induced enhancement of superconductivity, we performed the THz-THG experiment. Recently, the Higgs mode, i.e., the amplitude oscillation of the superconducting order parameter, was observed through the THz pump and THz probe experiment in an  $s$ -wave superconductor NbN<sup>39</sup>, and subsequently THz-THG mediated by the Higgs mode was demonstrated<sup>40</sup> (for a recent review, see ref. 41). The experimental scheme has been extended to  $d$ -wave cuprate superconductors<sup>42,43</sup> and multiband superconductors<sup>44,45</sup>. Here we investigated THz-THG in FeSe<sub>0.5</sub>Te<sub>0.5</sub> to extract the dynamics of the superconducting order parameter upon the photoexcitation. To measure the THz-THG signal from FeSe<sub>0.5</sub>Te<sub>0.5</sub>, a multicycle THz wave with the center photon energy of  $\hbar\omega = 2$  meV (0.5 THz in frequency) is focused onto the sample and the waveform of the transmitted THz pulse,  $E_{\text{tr}}(t)$ , is recorded as illustrated in Fig. 3a (also see “Methods”). Figure 3b shows  $E_{\text{tr}}(t)$  above and below  $T_c$  measured without photoexcitation, and the corresponding power spectra are plotted in the inset. Third

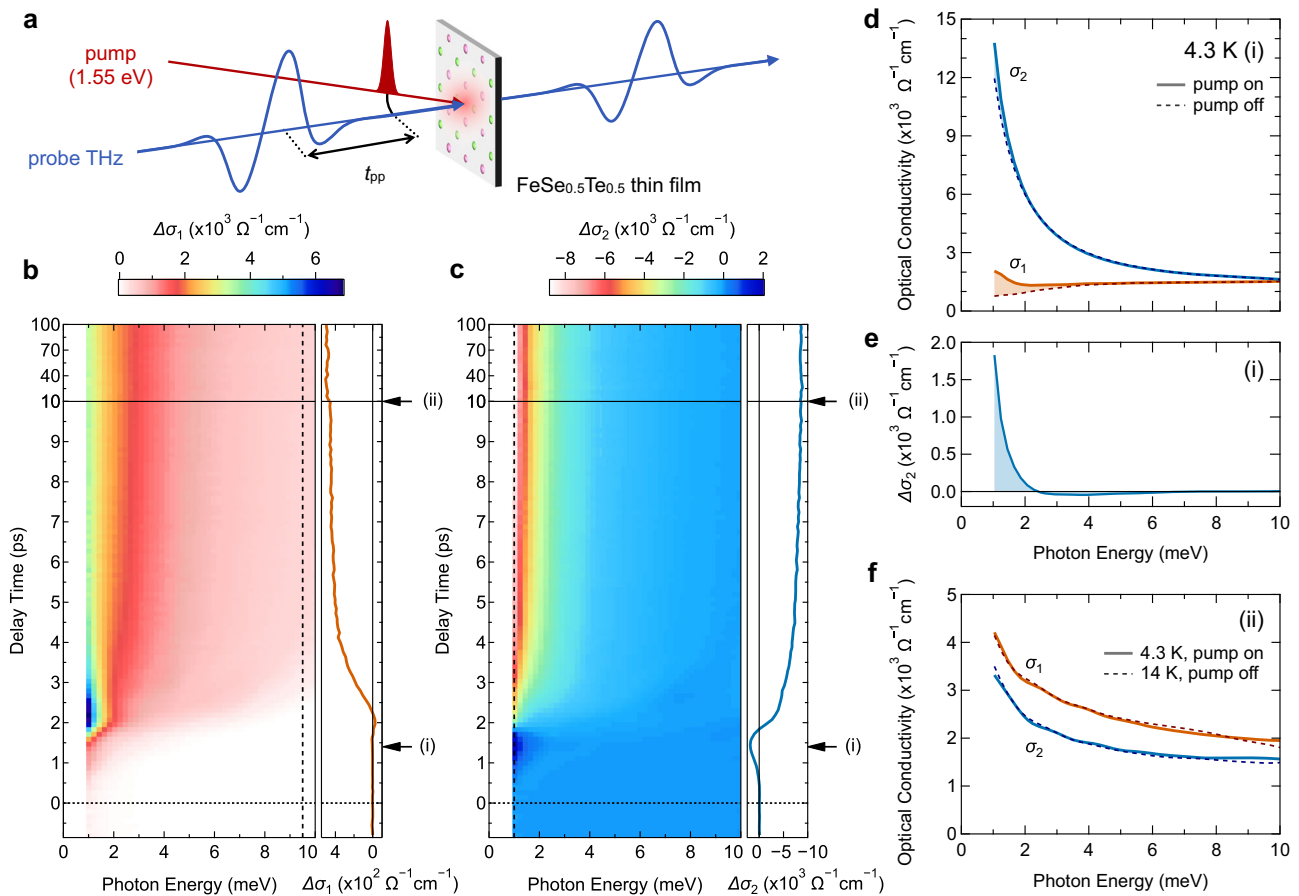


**Fig. 2** Transient optical conductivity of photoexcited FeSe<sub>0.5</sub>Te<sub>0.5</sub> below T<sub>c</sub>. **a** Schematic illustration of the optical pump-terahertz (THz) probe experiment. A near-infrared pump pulse is shown by red. **b, c** Time evolution of the pump-induced conductivity change,  $\Delta\tilde{\sigma}(\omega; t_{pp}) = \tilde{\sigma}(\omega; t_{pp}) - \tilde{\sigma}^{eq}(\omega)$  (**b**: real part; and **c**: imaginary part), where  $\omega$  is the angular frequency of the THz probe pulse and  $t_{pp}$  is the pump-probe delay time. Vertical dashed lines show the probe photon energies of **b**  $\hbar\omega_{probe} = 9.5$  meV and **c** 1.0 meV, at which  $\Delta\tilde{\sigma}(\omega_{probe}; t_{pp})$  are shown as functions of  $t_{pp}$  in their right panels. Black arrows denote (i)  $t_{pp} = 1.4$  ps and (ii) 10 ps, which correspond to **d-f**, respectively. Time origin ( $t_{pp} = 0$  ps), indicated by a black horizontal dotted line, is defined by the pump arrival time to the sample. The pump fluence was  $2.6 \mu\text{J cm}^{-2}$ . **d** Transient optical conductivities,  $\tilde{\sigma}(\omega; t_{pp})$ , at  $t_{pp} = 1.4$  ps (red: real part; and blue: imaginary part) and **e** the corresponding imaginary part of the differential optical conductivity,  $\Delta\sigma_2(\omega)$ . **f**  $\tilde{\sigma}(\omega; t_{pp})$  at  $t_{pp} = 10$  ps (red: real part; and blue: imaginary part).  $\tilde{\sigma}^{eq}(\omega)$  at 14 K are also shown by dashed lines.

harmonic (TH) signal is clearly identified both in the time-domain waveform and the power spectrum below T<sub>c</sub>. To discuss the temperature dependence of the THG efficiency, we evaluated the squared magnitude of the THG susceptibility,  $|\chi^{(3)}|^2 = I_{TH}/(I_F)^3$ , for each temperature, where  $I_{TH}$  and  $I_F$  are intensities of the observed TH (3 $\omega$ ) and fundamental ( $\omega$ ) signals, respectively (see Supplementary Note 3 for details of the analysis). As shown in Fig. 3c,  $|\chi^{(3)}|^2$  sharply increases below T<sub>c</sub>, indicating a clear correlation between the TH intensity and the superconductivity. In the case of multiband superconductors, multiple Higgs mode resonances are expected to occur at  $2\hbar\omega = 2\Delta_i(T)$  in the THG susceptibility with the band index  $i$ <sup>46</sup>, while the relative magnitude of the resonant peak depends on various parameters such as the impurity scattering rate and the gap energy<sup>47–51</sup>. In the present case, the resonance peak expected for the large gap at  $2\hbar\omega = 2\Delta_L(T)$  is absent (Fig. 3c) and seemingly only the small gap  $2\Delta_S(T)$  contributes to the THG signal. This tendency is consistent with the recent theoretical calculation<sup>50</sup>, though further detailed study taking into account the smallness of the Fermi energy and the effect of the strong electron correlation is needed, which remains a future issue. By neglecting the contribution from the large gap to the THG signal, we fit the temperature dependence of the THG susceptibility with that expected for the Higgs

mode in single-band s-wave superconductors<sup>52</sup>,

$$|\chi^{(3)}(T)|^2 \propto \frac{\Delta^4(T)}{[2\Delta(T) - 2\hbar\omega + i\gamma]}, \quad (1)$$

where we adapt  $\Delta_S(T)$  for  $\Delta(T)$  and  $\gamma$  is the phenomenological mode damping rate. Here we assume that the temperature dependence of the two superconducting gap energies is described by the coupled BCS gap equations with scaling T<sub>c</sub> (see Supplementary Note 4)<sup>53,54</sup>. As presented in Fig. 3c, the fitting with Eq. (1) shows a good agreement with the experimental result and provides the value of  $2\Delta(0) = 2.4$  meV, which is consistent with the measured spectral profile of the optical conductivity (Fig. 1c) and other measurements<sup>29,31–34</sup>. The simultaneously obtained large gap energy,  $2\Delta_L(0) = 8.0$  meV, provides a considerably large value of the ratio  $2\Delta_L/k_B T_c \sim 5.8$ , exceeding the weak-coupling limit of 3.53, in accordance with previous Andreev spectroscopy<sup>55,56</sup> and the magnetic penetration depth measurement by muon spin rotation technique<sup>57</sup>. One may also consider the effect of the charge density fluctuation (CDF) that also contributes to THG<sup>58</sup>. We do not rule out the contribution of CDF here, but it has been theoretically demonstrated that the light-Higgs coupling is drastically enhanced when the non-magnetic impurity scattering rate is comparable to the gap energy, i.e.,  $\gamma \sim \Delta$ <sup>47–50</sup> and gives a leading contribution to THz-

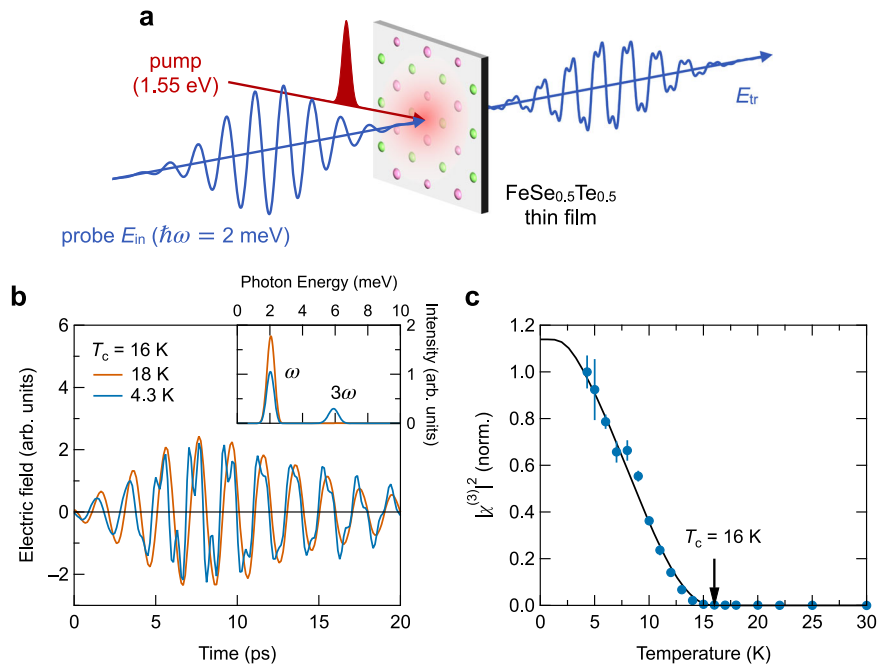


**Fig. 3 THz-THG signal from FeSe<sub>0.5</sub>Te<sub>0.5</sub> in equilibrium.** **a** Schematic illustration of the terahertz third-harmonic generation (THz-THG) measurement. Narrowband THz probe pulse with the center photon energy of  $\hbar\omega = 2$  meV (0.5 THz in frequency) is used. A near-infrared pump pulse, used for the photoexcitation, is also shown by red. The results shown in **b**, **c** are obtained without the pump pulse. **b** Time-domain waveform of the transmitted THz pulses at 18 and 4.3 K (red and blue, respectively), along with the power spectra shown in the inset. 1.5 THz bandpass filters are inserted after the sample to reduce the transmitted fundamental component. **c** Temperature dependence of the squared magnitude of the THG susceptibility,  $|\chi^{(3)}|^2 = I_{\text{TH}}/(I_{\text{F}})^3$ , with intensities of the observed TH and fundamental signals,  $I_{\text{TH}}$  and  $I_{\text{F}}$ . Error bars represent the standard deviation. The fit curve by assuming the Higgs mode response represented by Eq. (1) in the text is also shown by the solid line.

THG, the condition of which is satisfied in the present case of FeSe<sub>0.5</sub>Te<sub>0.5</sub>. Importantly, the THG signal exhibits a clear correlation with superconductivity as manifested by the temperature dependence of  $|\chi^{(3)}|^2$ . This result allows us to utilize the THG signal as an indicator of the superconducting order parameter.

**The photoexcitation effect of superconductivity probed by THG.** Next, we measured THz-THG under the photoexcitation to investigate the nonequilibrium dynamics of superconductivity. We irradiated a multicycle THz pulse for THG (hereinafter referred to as THz probe pulse) and a NIR excitation pulse (hereinafter referred to as pump pulse) simultaneously to the sample and measured the waveform of the transmitted THz probe pulse, as illustrated in Fig. 3a. Figure 4a shows the waveform of the THG signal, transmitted through the sample at 4.3 K. Here we analytically extracted the TH frequency component of 1.5 THz from the measured waveform. The arrival time of the NIR pump pulse, denoted by the black arrow, is  $t = 3.5$  ps. One sees that the TH signal is enhanced in the initial 2 ps after the photoexcitation and then suppressed. This dynamics of the TH signal reflects the enhancement and suppression of the superconducting order parameter associated with the small gap.

In this measurement, the relative time between the pump and probe pulse was fixed so that the temporal resolution of the photoexcitation dynamics was limited by the frequency of 1.5 THz ( $\sim 0.7$  ps in time)<sup>59,60</sup>. Next, we measured the THG susceptibility under the NIR pump by scanning the probe pulse with keeping the timing of the sampling pulse fixed: in such a case, the time resolution is not restricted by the period and the duration of the THz probe pulse but mostly determined by the pulse duration of the NIR sampling pulse of  $\sim 140$  fs (see “Methods” for details). Figure 4b displays the TH waveforms of

the THz probe pulses at the indicated delay times after the photoexcitation. As shown in Fig. 4c, the TH intensity normalized by its equilibrium value increases and reaches maximum at  $t_{\text{pp}} = 1.4$  ps, followed by the gradual reduction. At  $t_{\text{pp}} > 5$  ps, the TH intensity becomes about 1% of that in equilibrium, indicating that the superconductivity is mostly destroyed, and the system thermalizes to a normal metallic state. The time evolution of the THG signal can be compared by the numerical calculation of the THG signal by assuming the time-dependent superconducting order parameter (Fig. 4d, e). Since we adopted two measurement schemes in our optical pump and THz-THG probe experiments, i.e., one is to track the real-time dynamics of the THz electromagnetic wave (Fig. 4a) and the other is to track the dynamics of the superconducting order parameter by measuring the THG intensity as a function of  $t_{\text{pp}}$  (Fig. 4b, c), we utilized two kinds of the procedures to obtain the corresponding numerical results (details are given in Supplementary Note 5). The experimentally observed enhancement of the THG signal is well reproduced by the calculations, from which the amount of the photoinduced enhancement of the small gap is estimated to be 10%.

It is remarkable that the dynamics of the THG signal shows a good agreement with the result of the transient optical conductivity measurement. These results corroborate the photo-induced enhancement of the superconducting order parameter and the resulting enhancement of the superfluid density. At  $t_{\text{pp}} = 1.4$  ps where the THG signal is maximized, we also observed an increase of  $\sigma_2$  by the amount of about 10%, which is equivalent to the gap enhancement of the hole bands evaluated from the THG measurements. Since the divergent  $\sigma_2$  spectrum consists of the superfluid densities of both the electron and hole bands, this result indicates that  $\sigma_2$  in the low-energy region contains a

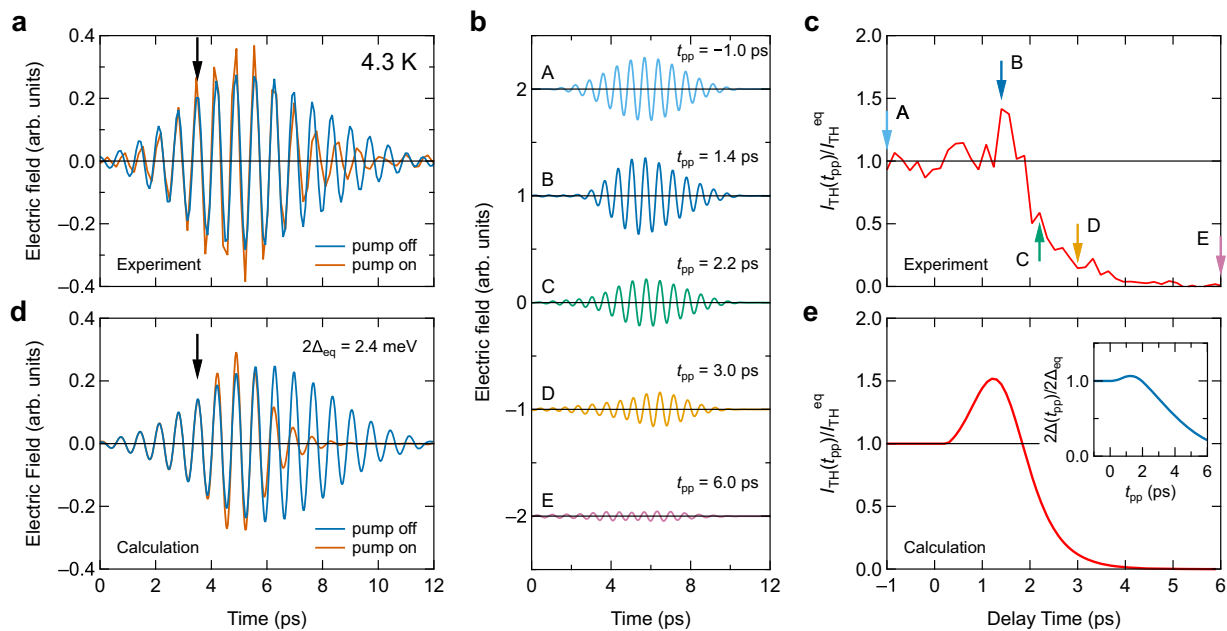


**Fig. 4 Time-resolved THz-THG signal under the photoexcitation.** **a** Waveform of the third harmonic (TH) component of the transmitted probe pulse. A black arrow at  $t = 3.5$  ps indicates the arrival time of the pump pulse to the sample. The pump fluence is  $2.6 \mu\text{J cm}^{-2}$ . **b** TH component of the terahertz field measured at fixed pump-probe delay times,  $t_{pp}$ , respectively. **c** Time evolution of the TH intensity,  $I_{TH}(t_{pp})$ , normalized by the TH intensity in equilibrium,  $I_{TH}^{eq}$ . Arrows indicate pump-probe delay times at which the TH waveforms shown in **b** were measured. **d** Calculated waveform of the TH signal and **e** time evolution of the TH intensity, which correspond to the experimental results shown in **a**, **c**, respectively. Time evolution of the superconducting gap energy after the photoexcitation normalized by the gap energy in equilibrium,  $2\Delta(t_{pp})/2\Delta_{eq}$ , which is used for the calculation, is shown in the inset.

substantial contribution of the superfluid density in the hole bands exhibiting the small gap, comparable to that in the electron bands exhibiting the large gap. Such disproportionality of the superfluid density with respect to the gap value has been identified in the FeSe superconductor<sup>61</sup>. We also confirmed that the enhancement of the THG signal, or to be precise the emergence of the THG signal, is not observed above  $T_c$  upon the photoexcitation (the data at 18 K are shown in Supplementary Fig. 2b), consistent with the transient optical conductivity measurement at  $T > T_c$ .

## Discussion

Now we address the role of the photoexcitation for the enhancement of the superconducting order parameter. One possible mechanism is the photoexcitation of coherent  $A_{1g}$  phonons through the Raman process that leads to the modulation of electronic band structures as reported in time-resolved ARPES<sup>22,62,63</sup> and the time-resolved X-ray measurement<sup>63</sup> in FeSe. However, the optical pump pulse in our experiments is at  $\sim 10 \mu\text{J cm}^{-2}$  per pulse, which is about two orders of magnitude smaller than those of previous experiments. The induced lattice modulation is estimated to the order of 0.01 pm, which is considerably small to cause the dynamical band structure modulation as observed in previous reports<sup>22,62,63</sup>. Besides, it is unlikely that the  $A_{1g}$  phonons ( $\hbar\omega \sim 20$  meV in the case of FeSe) are effectively excited by the excitation pulse with the pulse width of  $\sim 140$  fs (the bandwidth is  $\sim 23$  meV in photon energy). Photoinduced melting of the long-range nematic order is not relevant because it is absent in the present case of  $\text{FeSe}_{0.5}\text{Te}_{0.5}$ <sup>14</sup>. Combining with the thresholdless behavior of the transient signal (see Supplementary Note 6), we are left with a possible scenario that the observed enhancement of the superconducting order parameter is more directly related to the photo-carrier injection. The absorbed incident photon density is estimated as  $8 \times 10^{17} \text{ cm}^{-3}$  for the pump fluence of  $2.6 \mu\text{J cm}^{-2}$  (details are

given in Supplementary Note 7), which is more than two orders of magnitude smaller than the hole density in the hole pockets estimated from the Hall measurements in  $\text{FeSe}_{1-x}\text{Te}_x$  ( $x < 0.4$ )<sup>64</sup>. This estimation is also consistent with the real-part optical conductivity above  $T_c$  where the photoinduced increase of the spectral weight was  $< 1\%$  compared to that of equilibrium (Supplementary Fig. 2a). Notably, in our pump fluence regime, the transient optical conductivity in the high-energy region ( $\hbar\omega > 3$  meV) remains nearly unchanged upon the photoexcitation (Fig. 2b, c), which means that the photoexcitation has little effect on the electron bands in the initial temporal region ( $< 2$  ps) even in the superconducting phase. Therefore, one may infer that the injection of a fraction of carriers into the hole bands gives rise to the enhancement of superconductivity through the modification of interband pair scatterings. In fact, transport measurements of FeSe under high hydrostatic pressure have suggested that the increase of  $T_c$  is associated with the increase of the hole density and the enhancement of the interband spin fluctuations<sup>65</sup>. The significance of the interband anti-ferromagnetic fluctuation, and its cooperation with the orbital fluctuation, has been extensively studied as the origin of superconductivity in FeSCs<sup>66–70</sup>. In  $\text{FeSe}_{1-x}\text{Te}_x$  system, the correlation between the interband interaction in the  $d_{xy}$ -orbital channel and the enhancement of  $T_c$  has also been pointed out in recent ARPES study<sup>30</sup>. It should be noted here that the robustness of the superconductivity in the electron bands is considered to play a crucial role for the counterintuitive behavior that the superconductivity in the hole bands is enhanced despite the photocarrier injection into the hole bands. To examine this picture more quantitatively, we calculated the superconducting gaps from the coupled BCS gap equations analysis by implementing a 10% increase into the interband pairing interaction from the equilibrium value (see Supplementary Note 4). The results show a nearly same order ( $\sim 10\%$ ) increase for the small gap but an order of magnitude smaller change for the large gap, which reasonably agree with our experimental

observation. This picture is also consistent with the result that the enhancement of superconductivity is observed only below  $T_c$  in the investigated pump fluence regime (the data above  $T_c$  are shown in Supplementary Note 2), indicating the importance of the pre-existing condensate in the electron bands.

In summary, we demonstrate the transient enhancement of the superconducting order parameter in  $\text{FeSe}_{0.5}\text{Te}_{0.5}$  under the NIR optical pulse excitation. The enhancement of superconductivity is manifested by the enhancement of the imaginary part of the optical conductivity, which represents the superfluid density. The enhancement of the superconducting order parameter is further corroborated by the time-resolved THz-THG measurement, which is accounted for by the Higgs mode response. Remarkably, this result is contrary to the conventional understanding that the photoinjection of the quasiparticles suppresses superconductivity. By resolving the ultrafast dynamics between the two superconducting gaps in the terahertz frequency domain, we elucidate that the enhancement of superconductivity occurs only in the hole bands but not in the electron bands. This result is considered as an inherent character of the multiband superconductivity in  $\text{FeSe}_{0.5}\text{Te}_{0.5}$ , where the interband pairing interactions play an essential role. Moreover, the present result provides a route for the dynamical tuning of pairing interactions and resulting superconductivity in multiband superconductors by light. The time-resolved THz-THG adopted in this work provides a way to investigate nonequilibrium dynamics of the superconducting order parameter with picosecond time resolution and may be applied to investigate the light-induced superconducting phenomena.

## Methods

**Optical conductivity measurement.** The output from a regenerative amplified Ti:sapphire laser (pulse duration of 90 fs, central photon energy of  $\hbar\omega = 1.55$  eV, repetition rate of 1 kHz) was split into three pulses: one is for a NIR excitation pulse (pump pulse), another is to generate a broad-band THz wave (probe pulse), and the other is for a NIR sampling pulse for electro-optic (EO) sampling. We generated a broad-band (single-cycle) THz probe pulse from a *p*-type InAs (111) crystal illuminated with the NIR pulse. Time-domain waveform of the transmitted probe pulse was detected by EO sampling in a ZnTe (110) crystal with a thickness of 2 mm. To obtain the time-domain waveform of the probe pulse at each pump-probe delay time,  $t_{pp}$ , the temporal interval between a pump pulse and a sampling pulse was fixed to  $t_{pp}$  and the timing of probe pulse was swept. The NIR pump pulse duration is estimated to be 140 fs by an autocorrelation measurement.

**THz-THG measurement.** The output from the regenerative amplified Ti:sapphire laser was split into three pulses: one is for a NIR excitation pulse (pump pulse), another is to generate a multi-cycle THz wave for THG (probe pulse), and the other is for a NIR sampling pulse for EO sampling. By utilizing the tilted-pulse-front method with a LiNbO<sub>3</sub> crystal<sup>71,72</sup>, we generated an intense broad-band (single-cycle) THz pulse with the peak field of  $150 \text{ kV cm}^{-1}$ . To obtain the narrower bandwidth THz source with the center frequency of  $\omega/2\pi = 0.5 \text{ THz}$ , we placed four bandpass filters before the sample and the peak electric field is estimated as  $15 \text{ kV cm}^{-1}$  at the sample position inside the cryostat. To extract the TH signal with suppressing the fundamental 0.5 THz component, two 1.5 THz band-pass filters were inserted after the sample. Time-domain waveform of the probe pulse transmitted through the sample was detected by EO sampling in a ZnTe (110) crystal with a thickness of 2 mm.

In the photoexcitation measurement with a NIR pump pulse, the real-time waveform of the THz wave shown in Fig. 4a is obtained by fixing the timing of the pump pulse and the probe pulse and sweeping the arrival time of the sampling pulse. On the other hand, time-domain waveforms of probe pulses at fixed pump-probe delay times shown in Fig. 4b are obtained by fixing the time delay between the pump pulse and the sampling pulse and sweeping the timing of the probe pulse. With this procedure, we obtained the probe THz waveform, and every point of the waveform is measured with a fixed delay time after the photoexcitation. In the procedure, pump-probe delay time,  $t_{pp}$ , is defined as the time interval between the pump pulse and the sampling pulse. The latter method has been demonstrated to provide information about a transient state after photoexcitation unless the rise time is shorter than the pulse duration of the sampling pulse<sup>59,60,73</sup>.

## Data availability

The data that support the findings of this study are available from the corresponding author upon reasonable request.

Received: 12 January 2021; Accepted: 22 June 2021;

Published online: 14 July 2021

## References

- Kamihara, Y. et al. Iron-based layered superconductor:  $\text{LaOFeP}$ . *J. Am. Chem. Soc.* **128**, 10012–10013 (2006).
- Shibauchi, T., Carrington, A. & Matsuda, Y. A quantum critical point lying beneath the superconducting dome in iron pnictides. *Annu. Rev. Condens. Matter Phys.* **5**, 113–135 (2014).
- Kreisel, A., Hirschfeld, P. J. & Andersen, B. M. On the remarkable superconductivity of FeSe and its close cousins. *Symmetry* **12**, 1402 (2020).
- Shibauchi, T., Hanaguri, T. & Matsuda, Y. Exotic superconducting states in FeSe-based materials. *J. Phys. Soc. Jpn.* **89**, 102002 (2020).
- Sun, J. P. et al. Dome-shaped magnetic order competing with high-temperature superconductivity at high pressures in FeSe. *Nat. Commun.* **7**, 12146 (2016).
- Guo, J. et al. Superconductivity in the iron selenide  $\text{K}_x\text{Fe}_2\text{Se}_2$  ( $0 \leq x \leq 1.0$ ). *Phys. Rev. B* **82**, 180520 (2010).
- Miyata, Y., Nakayama, K., Sugawara, K., Sato, T. & Takahashi, T. High-temperature superconductivity in potassium-coated multilayer FeSe thin films. *Nat. Mater.* **14**, 775–779 (2015).
- Lei, B. et al. Evolution of high-temperature superconductivity from a low- $T_c$  phase tuned by carrier concentration in FeSe thin flakes. *Phys. Rev. Lett.* **116**, 077002 (2016).
- Kouno, S. et al. Superconductivity at 38 K at an electrochemical interface between an ionic liquid and  $\text{FeSe}_{0.8}\text{Te}_{0.2}$  on various substrates. *Sci. Rep.* **8**, 14731 (2018).
- Liu, D. et al. Electronic origin of high-temperature superconductivity in single-layer FeSe superconductor. *Nat. Commun.* **3**, 931 (2012).
- He, S. et al. Phase diagram and electronic indication of high-temperature superconductivity at 65 K in single-layer FeSe films. *Nat. Mater.* **12**, 605–610 (2013).
- Ge, J.-F. et al. Superconductivity above 100 K in single-layer FeSe films on doped  $\text{SrTiO}_3$ . *Nat. Mater.* **14**, 285–289 (2015).
- Hosoi, S. et al. Nematic quantum critical point without magnetism in  $\text{FeSe}_{1-x}\text{S}_x$  superconductors. *Proc. Natl Acad. Sci. USA* **113**, 8139–8143 (2016).
- Imai, Y. et al. Control of structural transition in  $\text{FeSe}_{1-x}\text{Te}_x$  thin films by changing substrate materials. *Sci. Rep.* **7**, 46653 (2017).
- Hanaguri, T. et al. Two distinct superconducting pairing states divided by the nematic end point in  $\text{FeSe}_{1-x}\text{S}_x$ . *Sci. Adv.* **4**, eaar6419 (2018).
- Nabeshima, F., Ishikawa, T., Oyanagi, K., Kawai, M. & Maeda, A. Growth of superconducting epitaxial films of sulfur substituted FeSe via pulsed laser deposition. *J. Phys. Soc. Jpn.* **87**, 073704 (2018).
- Shi, X. et al. Enhanced superconductivity accompanying a Lifshitz transition in electron-doped FeSe monolayer. *Nat. Commun.* **8**, 14988 (2017).
- Kim, K. W. et al. Ultrafast transient generation of spin-density-wave order in the normal state of  $\text{BaFe}_2\text{As}_2$  driven by coherent lattice vibrations. *Nat. Mater.* **11**, 497–501 (2012).
- Luo, C.-W. et al. Unveiling the hidden nematicity and spin subsystem in FeSe. *npj Quant. Mater.* **2**, 32 (2017).
- Konstantinova, T. et al. Photoinduced dynamics of nematic order parameter in FeSe. *Phys. Rev. B* **99**, 180102(R) (2019).
- Shimojima, T. et al. Ultrafast nematic-orbital excitation in FeSe. *Nat. Commun.* **10**, 1946 (2019).
- Suzuki, T. et al. Photoinduced possible superconducting state with long-lived disproportionate band filling in FeSe. *Commun. Phys.* **2**, 115 (2019).
- Fausti, D. et al. Light-induced superconductivity in a stripe-ordered cuprate. *Science* **331**, 189–191 (2011).
- Kaiser, S. et al. Optically induced coherent transport far above  $T_c$  in underdoped  $\text{YBa}_2\text{Cu}_3\text{O}_{6+\delta}$ . *Phys. Rev. B* **89**, 184516 (2014).
- Liu, B. et al. Pump frequency resonances for light-induced incipient superconductivity in  $\text{YBa}_2\text{Cu}_3\text{O}_{6.5}$ . *Phys. Rev. X* **10**, 011053 (2020).
- Mitrano, M. et al. Possible light-induced superconductivity in  $\text{K}_3\text{C}_{60}$  at high temperature. *Nature* **530**, 461–464 (2016).
- Cantaluppi, A. et al. Pressure tuning of light-induced superconductivity in  $\text{K}_3\text{C}_{60}$ . *Nat. Phys.* **14**, 837–841 (2018).
- Buzzi, M. et al. Photomolecular high-temperature superconductivity. *Phys. Rev. X* **10**, 031028 (2020).
- Miao, H. et al. Isotropic superconducting gaps with enhanced pairing on electron Fermi surfaces in  $\text{FeTe}_{0.55}\text{Se}_{0.45}$ . *Phys. Rev. B* **85**, 094506 (2012).

30. Nakayama, K. et al. Orbital mixing at the onset of high-temperature superconductivity in  $\text{FeSe}_{1-x}\text{Te}_x/\text{CaF}_2$ . *Phys. Rev. Res.* **3**, L012007 (2021).
31. Homes, C. C. et al. Electronic correlations and unusual superconducting response in the optical properties of the iron chalcogenide  $\text{FeTe}_{0.55}\text{Se}_{0.45}$ . *Phys. Rev. B* **81**, 180508 (2010).
32. Homes, C. C., Dai, Y. M., Wen, J. S., Xu, Z.-J. & Gu, G.-D.  $\text{FeTe}_{0.55}\text{Se}_{0.45}$ : a multiband superconductor in the clean and dirty limit. *Phys. Rev. B* **91**, 144503 (2015).
33. Hanaguri, T., Niitaka, S., Kuroki, K. & Takagi, H. Unconventional *s*-wave superconductivity in  $\text{Fe}(\text{Se},\text{Te})$ . *Science* **328**, 474–476 (2010).
34. Machida, T. et al. Zero-energy vortex bound state in the superconducting topological surface state of  $\text{Fe}(\text{Se},\text{Te})$ . *Nat. Mater.* **18**, 811–815 (2019).
35. Kennes, D. M., Wilner, E. Y., Reichman, D. R. & Millis, A. J. Transient superconductivity from electronic squeezing of optically pumped phonons. *Nat. Phys.* **13**, 479–483 (2017).
36. Ahn, J. & Nagaosa, N. Theory of optical responses in clean multi-band superconductors. *Nat. Commun.* **12**, 1617 (2021).
37. Barankov, R. A., Levitov, L. S. & Spivak, B. Z. Collective Rabi oscillations and solitons in a time-dependent BCS pairing problem. *Phys. Rev. Lett.* **93**, 160401 (2004).
38. Sentef, M. A., Kemper, A. F., Georges, A. & Kollath, C. Theory of light-enhanced phonon-mediated superconductivity. *Phys. Rev. B* **93**, 144506 (2016).
39. Matsunaga, R. et al. Higgs amplitude mode in the BCS superconductors  $\text{Nb}_{1-x}\text{Ti}_x\text{N}$  induced by terahertz pulse excitation. *Phys. Rev. Lett.* **111**, 057002 (2013).
40. Matsunaga, R. et al. Light-induced collective pseudospin precession resonating with Higgs mode in a superconductor. *Science* **345**, 1145–1149 (2014).
41. Shimano, R. & Tsuji, N. Higgs mode in superconductors. *Annu. Rev. Condens. Matter Phys.* **11**, 103–124 (2020).
42. Katsumi, K. et al. Higgs mode in the *d*-wave superconductor  $\text{Bi}_2\text{Sr}_2\text{CaCu}_2\text{O}_{8+x}$  driven by an intense terahertz pulse. *Phys. Rev. Lett.* **120**, 117001 (2018).
43. Chu, H. et al. Phase-resolved Higgs response in superconducting cuprates. *Nat. Commun.* **11**, 1793 (2020).
44. Kovalev, S. et al. Band-selective third-harmonic generation in superconducting  $\text{MgB}_2$ : evidence for Higgs amplitude mode in the dirty limit. Preprint at <https://arxiv.org/abs/2010.05019> (2020).
45. Vaswani, C. et al. Light quantum control of persisting Higgs modes in iron-based superconductors. *Nat. Commun.* **12**, 258 (2021).
46. Murotani, Y., Tsuji, N. & Aoki, H. Theory of light-induced resonances with collective Higgs and Leggett modes in multiband superconductors. *Phys. Rev. B* **95**, 104503 (2017).
47. Jujo, T. Quasiclassical theory on third-harmonic generation in conventional superconductors with paramagnetic impurities. *J. Phys. Soc. Jpn.* **87**, 024704 (2018).
48. Murotani, Y. & Shimano, R. Nonlinear optical response of collective modes in multiband superconductors assisted by nonmagnetic impurities. *Phys. Rev. B* **99**, 224510 (2019).
49. Silaev, M. Nonlinear electromagnetic response and Higgs-mode excitation in BCS superconductors with impurities. *Phys. Rev. B* **99**, 224511 (2019).
50. Haanel, R., Froese, P., Manske, D. & Schwarz, L. Time-resolved optical conductivity and Higgs oscillations in two-band dirty superconductors. Preprint at <https://arxiv.org/abs/2012.07674> (2020).
51. Tsuji, N. & Nomura, Y. Higgs-mode resonance in third harmonic generation in  $\text{NbN}$  superconductors: multiband electron-phonon coupling, impurity scattering, and polarization-angle dependence. *Phys. Rev. Res.* **2**, 043029 (2020).
52. Tsuji, N. & Aoki, H. Theory of Anderson pseudospin resonance with Higgs mode in superconductors. *Phys. Rev. B* **92**, 064508 (2015).
53. Suhl, H., Matthias, B. T. & Walker, L. R. Bardeen-Cooper-Schrieffer theory of superconductivity in the case of overlapping bands. *Phys. Rev. Lett.* **3**, 552–554 (1959).
54. Kuzmichev, S. A., Kuzmicheva, T. E. & Tchesnokov, S. N. Determination of the electron-phonon coupling constants from the experimental temperature dependences of superconducting gaps in  $\text{MgB}_2$ . *JETP Lett.* **99**, 295–302 (2014).
55. Kuzmicheva, T. E. et al. Andreev spectroscopy of iron-based superconductors: temperature dependence of the order parameters and scaling of  $\Delta_{1,2}$  with  $T_C$ . *Phys. Uspekhi* **57**, 819–827 (2014).
56. Kuzmicheva, T. E. et al. Direct evidence of two superconducting gaps in  $\text{FeSe}_{0.5}\text{Te}_{0.5}$ :  $\text{SnS}$ -Andreev spectroscopy and the lower critical field. *JETP Lett.* **104**, 852–858 (2016).
57. Bendele, M. et al. Anisotropic superconducting properties of single-crystalline  $\text{FeSe}_{0.5}\text{Te}_{0.5}$ . *Phys. Rev. B* **81**, 224520 (2010).
58. Cea, T., Castellani, C. & Benfatto, L. Nonlinear optical effects and third-harmonic generation in superconductors: Cooper pairs versus Higgs mode contribution. *Phys. Rev. B* **93**, 180507 (2016).
59. Kindt, J. T. & Schmittenmaier, C. A. Theory for determination of the low-frequency time-dependent response function in liquids using time-resolved terahertz pulse spectroscopy. *J. Chem. Phys.* **110**, 8589–8596 (1999).
60. Némec, H., Kadlec, F., Surendran, S., Kužel, P. & Jungwirth, P. Ultrafast far-infrared dynamics probed by terahertz pulses: a frequency domain approach. I. Model systems. *J. Chem. Phys.* **122**, 104503 (2005).
61. Li, M. et al. Superfluid density and microwave conductivity of  $\text{FeSe}$  superconductor: ultra-long-lived quasiparticles and extended *s*-wave energy gap. *N. J. Phys.* **18**, 082001 (2016).
62. Yang, S. et al. Thickness-dependent coherent phonon frequency in ultrathin  $\text{FeSe}/\text{SrTiO}_3$  films. *Nano Lett.* **15**, 4150–4154 (2015).
63. Gerber, S. et al. Femtosecond electron-phonon lock-in by photoemission and x-ray free-electron laser. *Science* **357**, 71–75 (2017).
64. Nabeshima, F., Ishikawa, T., Shikama, N. & Maeda, A. Correlation between superconducting transition temperatures and carrier densities in  $\text{Te}$ - and  $\text{S}$ -substituted  $\text{FeSe}$  thin films. *Phys. Rev. B* **101**, 184517 (2020).
65. Sun, J. P. et al. High- $T_c$  superconductivity in  $\text{FeSe}$  at high pressure: dominant hole carriers and enhanced spin fluctuations. *Phys. Rev. Lett.* **118**, 147004 (2017).
66. Mazin, I. I., Singh, D. J., Johannes, M. D. & Du, M. H. Unconventional superconductivity with a sign reversal in the order parameter of  $\text{LaFeAsO}_{1-x}\text{F}_x$ . *Phys. Rev. Lett.* **101**, 057003 (2008).
67. Suzuki, K. et al. Model of the electronic structure of electron-doped iron-based superconductors: evidence for enhanced spin fluctuations by diagonal electron hopping. *Phys. Rev. Lett.* **113**, 027002 (2014).
68. Linscheid, A., Maiti, S., Wang, Y., Johnston, S. & Hirschfeld, P. J. High  $T_c$  via spin fluctuations from incipient bands: application to monolayers and intercalates of  $\text{FeSe}$ . *Phys. Rev. Lett.* **117**, 077003 (2016).
69. Yamakawa, Y., Onari, S. & Kontani, H. Nematicity and magnetism in  $\text{FeSe}$  and other families of Fe-based superconductors. *Phys. Rev. X* **6**, 021032 (2016).
70. Benfatto, L., Valenzuela, B. & Fanfarillo, L. Nematic pairing from orbital-selective spin fluctuations in  $\text{FeSe}$ . *npj Quant. Mater.* **3**, 56 (2018).
71. Hebling, J., Almasi, G., Kozma, I. & Kuhl, J. Velocity matching by pulse front tilting for large area THz-pulse generation. *Opt. Express* **10**, 1161 (2002).
72. Watanabe, S., Minami, N. & Shimano, R. Intense terahertz pulse induced exciton generation in carbon nanotubes. *Opt. Express* **19**, 1528 (2011).
73. Orenstein, J. & Dodge, J. S. Terahertz time-domain spectroscopy of transient metallic and superconducting states. *Phys. Rev. B* **92**, 134507 (2015).

## Acknowledgements

We acknowledge the useful discussions with Y. Murotani, D. Manske, and L. Schwarz. This work was supported by JSPS KAKENHI (Grants Nos. 15H02102, 18H05324, 19K14625) and JST CREST Grant No. JPMJCR19T3, Japan. K.I. was supported by JSPS Research Fellowship for Young Scientists (Grant No. 20J22275) and JSR Fellowship, the University of Tokyo. J.W., on leave from Department of Physics and Astronomy, UBC, acknowledges the internship program of the Max Planck-UBC-UTokyo Centre.

## Author contributions

K.I., N.Y., K.K., and J.W. carried out the optical experiments and analyses. N.S., Y.S., F.N., and A.M. fabricated the thin film samples and performed the transport measurements. K.I. and R.S. wrote the manuscript with inputs from all co-authors. R.S. conceived the project. All the authors contribute to the discussion and interpretation of the results.

## Competing interests

The authors declare no competing interests.

## Additional information

**Supplementary information** The online version contains supplementary material available at <https://doi.org/10.1038/s42005-021-00663-8>.

**Correspondence** and requests for materials should be addressed to R.S.

**Peer review information** *Communications Physics* thanks the anonymous reviewers for their contribution to the peer review of this work.

**Reprints and permission information** is available at <http://www.nature.com/reprints>

**Publisher's note** Springer Nature remains neutral with regard to jurisdictional claims in published maps and institutional affiliations.



**Open Access** This article is licensed under a Creative Commons Attribution 4.0 International License, which permits use, sharing, adaptation, distribution and reproduction in any medium or format, as long as you give appropriate credit to the original author(s) and the source, provide a link to the Creative Commons license, and indicate if changes were made. The images or other third party material in this article are included in the article's Creative Commons license, unless indicated otherwise in a credit line to the material. If material is not included in the article's Creative Commons license and your intended use is not permitted by statutory regulation or exceeds the permitted use, you will need to obtain permission directly from the copyright holder. To view a copy of this license, visit <http://creativecommons.org/licenses/by/4.0/>.

© The Author(s) 2021